Using Satellite and ARM Observations to Evaluate Cold Air Outbreak Cloud Transitions in E3SM Global Storm-Resolving Simulations

X. Zheng[1], Y. Zhang[1], S. A. Klein[1], M. Zhang[1], Z. Zhang[2], M. Deng[3], J. Tian[1,5], C. R. Terai[1], B. Geerts[4], P. Caldwell[1], P. A. Bogenschutz[1]

[1]Cloud Processes Research and Modeling Group, Lawrence Livermore National Laboratory, Livermore, CA, USA
[2]Physics Department, University of Maryland Baltimore County, Baltimore, 21250, MD, USA
[3]Environmental and Climate Sciences Department, Brookhaven National Laboratory, Upton, NY, USA
[4]Department of Atmospheric Sciences, University of Wyoming, Laramie, WY, USA
[5]Pacific Northwest National Laboratory, Richland, WA, USA

Key Points:

- The Simple Cloud-Resolving E3SM Atmosphere Model (SCREAMv0), at a resolution of 3 km, simulated three distinctive cloud regimes in cold air outbreaks with credible mesoscale structures.
- SCREAMv0 qualitatively captures the transition of the cloud phase partitioning based on high-resolution observations.
- Observations selected based on large-scale conditions can be important references for global storm-resolving model evaluation.

Corresponding author: Xue Zheng, `zheng7@llnl.gov`

Abstract

This study evaluates the performance of a global storm-resolving model (GSRM), the Simple Cloud-Resolving E3SM Atmosphere Model (SCREAM). We analyze marine boundary layer clouds in a cold air outbreak over the Norwegian Sea in a 40-day simulation, and compare them to observations from satellite and a field campaign of the Atmospheric Radiation Measurement program (ARM). SCREAM qualitatively captures the cold air outbreak cloud transition in terms of the boundary layer growth, cloud mesoscale structure, and phase partitioning. SCREAM also correctly locates the greatest ice and liquid in the mesoscale updraft. However, the study finds that SCREAM might underestimate cloud supercooled liquid water in the cumulus cloud regime.

This study showcases the promise of employing high-resolution and high-frequency observations under similar large-scale conditions for evaluating GSRMs. This approach can help identify model features for future process-level studies before allocating extra resources for a time-matched model intercomparison of a specific case.

Plain Language Summary

Cold air outbreaks occur when cold, dry air moves over warmer ocean regions, forming extensive boundary layer clouds. However, current climate models struggle to accurately represent these clouds due to their complex nature. This study examines the performance of the global storm-resolving model, the Simple Cloud-Resolving E3SM Atmosphere Model (SCREAM), in simulating marine boundary layer clouds during cold air outbreaks over the Norwegian Sea. This study compares the SCREAM simulated clouds during a cold air outbreak event to observations under similar large-scale conditions from satellites and ground-based measurements collected during a field campaign of the Atmospheric Radiation Measurement program. The results indicate that SCREAM successfully simulates three distinct cloud patterns during cold air outbreaks with credible mesoscale structures. Yet, it tends to underestimate supercooled liquid water and consequently, the cloud liquid water fraction, especially in cumulus clouds. The study suggests that using high-resolution observations under similar large-scale conditions can effectively evaluate global storm-resolving models. This approach helps identify areas for improvement without requiring expensive global storm-resolving model simulation designed for specific cases.

1 Introduction

Marine cold-air outbreaks (MCAO) are characterized by the advection of cold and dry air masses over much warmer ocean (Pithan et al., 2018). Intense MCAOs often originate in polar regions and generate extensive boundary layer clouds (Papritz & Spengler, 2017). The MCAO cloud micro/macro-physical transition and mesoscale variability can lead to marked changes in the cloud radiative effects (Field et al., 2014). Yet, current climate models and numerical weather prediction models poorly capture MCAO clouds and clouds in the postfrontal cold sector in general (e.g., Field et al., 2017; Forbes & Ahlgrimm, 2014; Naud et al., 2019), because the operating scales of shallow convection and the related mixed-phase cloud processes are much finer than the model effective resolution.

Recent advances in computing have enabled the development of global storm resolving models (GSRMs) with kilometer-scale grid spacing as an invaluable and feasible complement to traditional climate models (e.g., Satoh et al., 2019; Stevens et al., 2019; Neumann et al., 2019). At this frontier, the U.S. Department of Energy (DOE) Energy Exascale Earth System Model (E3SM) project released its GSRM, the Simple Cloud-Resolving E3SM Atmosphere Model (SCREAM) version 0 (v0), at 3.25 km resolution (Caldwell et al., 2021). The great advantage of GSRMs is the explicit representations

of mesoscale variabilities, such as the cloud transition in MCAOs. However, even kilometer-scale models still struggle to represent detailed MCAO cloud macrophysics, due to the sub-grid-scale parameterized turbulence and microphysical processes and their tight interactions with the resolved-scale dynamics and physics that cannot be parameterized independently (e.g., Field et al., 2014, 2017).

The field campaign called Cold-Air Outbreaks in the Marine Boundary Layer Experiment (COMBLE) was held by the US DOE Atmospheric Radiation Measurement (ARM) program in 2020 over the northern Atlantic Ocean (Geerts et al., 2022). ARM ground-based observations during COMBLE, along with pixel-level satellite retrievals, provide valuable fine-scale observations for evaluating the resolved mesoscale variations and sub-grid cloud-scale processes in GSRMs. However, a direct time-matched comparison is impossible because, without data assimilation nor nudging to reanalysis, atmospheric large-scale states in global free runs naturally drift apart from observations after 5 days (Ma et al., 2014). Therefore, this study explores an alternative strategy by performing comparisons between clouds in SCREAM and those observed under similar large-scale conditions. The goal of this paper is to establish a qualitative diagnosis of general model biases in cloud processes during MCAOs with similar large-scale features. Thus, this work sets an exploratory stage for model bias identification, and provides guidance for the future in-depth process-oriented model sensitivity studies to trace model error sources and improve SCREAM performance.

The paper is organized as follows. The SCREAMv0 40-day global simulation and COMBLE observations are briefly described in section 2. Section 3 evaluates model performance on cloud mesoscale variability and phase partitioning. The final section presents discussion and conclusions.

2 Model simulation and observations

2.1 SCREAMv0 simulation

This study analyzes the SCREAMv0 40-day global simulation at 3.25 km grid spacing with prescribed SST and sea ice between 20 January and 1 March 2020 (Caldwell et al., 2021). This simulation produced ~ 4.5 TB output data per simulated day, which are regridded to 0.05^o lat–lon grids. SCREAMv0 adopts Simplified Higher Order Closure (SHOC; P. Bogenschutz & Krueger, 2013) as the turbulence scheme and the Predicted Particle Properties (P3; Morrison & Milbrandt, 2015) as the cloud microphysics scheme. P3 uses one single category for ice, in which the ice water variables, such as water path (IWP) and mixing ratio (q_i), include both cloud and precipitating ice (snow and graupel). The model liquid water path (LWP) here also includes rain water path to be more consistent with the definition of model IWP and ARM LWP retrievals. For further model details, please refer to Supporting Information.

2.2 Observational data

The ARM Mobile Facility (AMF1) of COMBLE was deployed at a coastal site near Andenes in northern Scandinavia (69^oN, 16^oE) between 1 December 2019 and 31 May 2020 (Geerts et al., 2022). The Active Remotely-Sensed Cloud Locations (ARSCL) product (Kollias et al., 2007) is used for the cloud structure analysis and the hourly total cloud fraction (Xie et al., 2010). To quantify the cloud phase partition, the cloud liquid water fraction is defined as the ratio of LWP to (LWP+IWP), in which LWP measurements are from microwave radiometer (Cadeddu et al., 2013) and IWP retrievals are based on cloud radar and lidar data (Deng et al., 2022). Furthermore, cloud top temperatures are calculated using the observed cloud top heights and 6-hourly radiosonde soundings (Holdridge, 2020; Hu, Lebo, et al., 2023). To minimize uncertainties in such calculation, we only in-

clude data within a one-hour window of the radiosonde launching time for evaluating the relationship between cloud top temperature and cloud liquid fraction.

Since COMBLE AMF1 was located (Fig. 1a) more than 1000 km away from the sea-ice edge, it only observed the downstream cumulus regime during MCAOs. To capture the cloud transition over the open ocean (Fig. 2), we use satellite data from Moderate Resolution Imaging Spectroradiometer (MODIS), CloudSat, and Cloud-Aerosol Lidar and Infrared Pathfinder Satellite Observations (CALIPSO). The pixel-level cloud retrievals are available with similar spatial resolutions as in SCREAMv0, which include cloud top temperature, cloud masks, cloud top phase, whole cloud phase, and the vertical profiles of radar reflectivity (Sassen et al., 2008; Marchand et al., 2008). There are five satellite paths capturing the cloud transition during the selected MCAO days in the COMBLE region (Fig. S5).

2.3 Selection of MCAO cases for model-observation comparison

To compare SCREAMv0 clouds with observations, we identify MCAO events using an MCAO index (M), where M represents the difference between the surface skin and 800 hPa potential temperature ($M = \theta_s - \theta_{800hPa}$). MCAO events are characterized by a positive M index in the COMBLE region(1^oW-17^oE,63^oN-80^oN) and prevailing northwesterly surface winds around the Norwegian coast (Fletcher et al., 2016; Geerts et al., 2022).

In the 40-day SCREAMv0 global simulation, the most intense simulated MCAO event in the COMBLE region occurs from Day 33 to Day 36 and peaks on Day 34 (Fig. S1). Daily-mean maps (Fig. 1) of surface conditions on Day 34 confirm that a low pressure system just passed north of the Norwegian coast with the majority of the Norwegian Sea is experiencing strong northwesterly surface wind. Along the large-scale flow from the Arctic sea-ice edge to the Norwegian coast, the M index exceeds $5K$ with a peak value of $\sim 10K$. The lowest model level wind speed exceeds 10 ms^{-1} and even reaches 16 ms^{-1}. As a result, the daily-mean sensible heat flux is higher than 450 Wm^{-2} right off the sea-ice edge and gradually reduces to $\sim 100\ Wm^{-2}$ near the Norwegian coast, whereas the latent heat flux is higher than 150 Wm^{-2} with a maximum region of ~ 250 Wm^{-2} north of the Norwegian coast. These maps all indicate a typical large-scale environment of intense MCAOs (Geerts et al., 2022; Pithan et al., 2018).

Because the SCREAMv0 simulation is a free run without constraining the large-scale circulations towards observations, the large-scale atmospheric conditions on Day 34 have drifted away from the observed states matching the simulated period. To address this temporal mismatch, we selected observational cases with the similar large-scale conditions as those on Day 34. Such selection is based on the combined root-mean-square error (RMSE) and Pearson correlation coefficient of daily-mean sea-level pressure, 2-m air temperature, 700-hPa geopotential height, and 500-hPa geopotential height between the SCREAMv0 Day 34 and ERA5 data in February and March, 2020 (Fig. S2a). The large-scale condition on 28 March 2020 (Fig. S3) is found to be the closest match to that on Day 34 (Fig. 1). In addition, the magnitude and distribution of the M index across the Norwegian Sea shown in Fig. 1b is very similar to that on 28 March 2020 (Fig. S3a and Fig. 2 in Geerts et al., 2022). Therefore, to examine the general behavior of cloud regime transition, cloud observations from 28 March 2020 (Fig. 2) are used as the observational reference to compare with the instantaneous cloud fields on Day 34 (Fig. 3).

Meanwhile, in the SCREAMv0 simulation the large-scale conditions on Day 33 show the highest similarity to those on Day 34 (Fig. S2b, Fig. S4). In observations, MCAOs on March 19, 20, 27, and 29 all bear similarities to the conditions on March 28, 2020 (Fig. S2a). In the following, observations from March 19, 20, 27, 28 and 29 are used to evaluate the statistical features of the detailed cloud phase partitions, and their interaction with dynamics on Day 33 and 34 (Fig. 4-5).

3 Results

3.1 Cloud morphology transition

The large-scale cloud field associated with intense MCAO events usually consists of three different regimes. Clouds offshore of the sea-ice edge are overcast BL clouds embedded with fine-scale cloud rolls. As the large-scale air mass moves southward to the open ocean, the clouds grow deeper and become more distinctive cloud streets with plenty of supercooled cloud liquid (Tornow et al., 2021). Over the downstream region near the coast, the clouds transition to less organized open-cellular clouds, and eventually ice-dominated cumulus clouds that may be 4-5 km deep (e.g., McCoy et al., 2017; Lloyd et al., 2018; Geerts et al., 2022; Wu & Ovchinnikov, 2022).

The MCAO on 28 March 2020 (Fig. 1f) is a typical example of such cloud transition. The snapshot of the simulated SWCRE on Day 34 at 1200UTC [12-13 local standard time (LST)] demonstrates that SCREAMv0 is capable of generating all three regimes: overcast shallow BL cloud deck, cloud streets and scattered cumulus clouds (Fig. 1c). The vertical cross-section along the red dashed line in Fig. 3a covers the regime transition, whose mesoscale cloud structure is demonstrated with model instantaneous cloud variables (Fig. 3).

In the upstream overcast BL cloud region (e.g., north of 75 ^{o}N in Fig. 1c, and the first 500 km of the vertical cross-section in Fig. 3), while many km-scale models often tend to underestimate cloud fraction and the related cloud radiative forcing (Field et al., 2017), SCREAMv0 faithfully reproduces a homogeneous overcast stratocumulus cloud deck (Fig. 1c), although lacking fine-scale cloud roll structures when compared with the MODIS reflectance (Fig. 1f). The simulated planetary boundary layer (PBL) originates below 1 km and gradually grows to near 2 km in depth (Fig. 3c), consistent with the observed clouds in the same regime (Fig. 2b). The cloud top temperature, defined as the model air temperature at the top of the cloud layer, is $\sim -20 - -25^{o}C$ (Fig. 3b,d). A thin supercooled liquid cloud layer exists at the top of the PBL with ice-phase hydrometeors falling out of the cloud layer (Fig. 3c). The solid cloud layer is maintained by subgrid PBL turbulent processes, given the weak model-resolved vertical velocity ($< \pm 0.5$ Pa/s in Fig. 3e). All these imply that SHOC (P. Bogenschutz & Krueger, 2013) effectively represents the PBL turbulence and BL clouds generated in strong offshore flows with significant sensible heat flux and lower-troposphere instability (Field et al., 2014).

Between $\sim 550 - 700$ km of the vertical cross-section, the cloud streets emerge in SCREAMv0 as the PBL deepens to above $2km$ and the resolved updrafts and downdrafts intensify ($> \pm 3.5 Pa/s \sim \pm 0.3 m/s$ Fig. 3e,f). Within this regime, the supercooled liquid cloud layer breaks up with reduced peak cloud water content (Fig. 3c,d) and the ice underneath intensifies and collocates with the resolved updrafts (Fig. 3e,f). The daily-mean cloud structures also show a cloud top deepening with decreasing supercooled liquid clouds (Fig. 1g). While clouds extend higher, cloud top temperatures remain similar to those of the overcast cloud regime due to the continuous warming of the PBL by the surface sensible and latent heat. The model vertical cross-sections, both along and across the clouds streets (Fig. 3e,f), reveal organized secondary circulations, which consist of a strong updraft within each convective cloud cell and compensating subsidence between cells (Gryschka & Raasch, 2005; Brümmer, 1999). These convective cells align with wind direction to form cloud streets, while the strong subsidence between streets cause the clouds to break up. Compared with the upstream overcast clouds off the sea-ice edge, more individual cloud cells appear along the CloudSat orbit indicating the scale of the observed convective clouds is increased (Fig. 2b).The simulated cloud streets (Fig. 1c,f) are wider (15-50 km) compared to observed streets (5-10 km). This difference may be attributed to the typical aspect ratio of roll convection in MCAOs ranging from 2 to 10 (e.g., Brümmer, 1999; Yang & Geerts, 2006). Given SCREAMv0's effective resolu-

218 tion ($\sim$ 15 km, Caldwell et al., 2021), a convective mixed layer depth of approximately
219 2 km is required for distinct rolls to form.

220   Surface sensible heat flux decreases and latent heat flux increases along the northwest-
221 to-southeast flow towards the Scandinavian coast (Fig. 1d,e). This leads to the breakup
222 of organized cloud streets and their transition into scattered cumulus clouds with sim-
223 ilar spatial sizes but clearer edges compared to observed cumulus clouds in the MODIS
224 reflectance (Fig. 1c,f). These simulated cumulus clouds, deeper than the upstream cloud
225 streets, are primarily composed of ice (Fig. 3a,b). At the end of the cross-section, the
226 simulated cloud-top height is $\sim$ 3 km, and the cloud top temperatures exhibit clear fluc-
227 tuations, occasionally dropping as low as $-30^o C$ (Fig. 3b,c).

228   The SCREAMv0 daily mean cloud-top height, estimated from daily mean q_i and
229 q_c, is slightly lower than the median value of hourly ARM cloud top heights(Fig. 1g) in
230 the region. Additionally, the SCREAM0 daily-mean cloud cover ($\sim 0.85-0.9$, depicted
231 as the black line in Fig. 1 h) is close to the range of the ARM hourly cloud cover ($\sim 0.82-$
232 1). The simulated daily mean IWP aligns with the observed median value, whereas the
233 simulated daily mean LWP is significantly lower than the 25 percentile of ARM hourly
234 LWPs (Fig. 1i). Consistently, the daily mean simulated cloud liquid water fraction in
235 this area is ~ 0.07 (Fig. 1h), notably lower than he observed variability range of 0.23
236 to 0.48 based on hourly data (Fig. 1i). Furthermore, an uncertainty analysis consider-
237 ing observational uncertainties (supporting information for details) in ARM IWP and
238 LWP suggests that daily mean cloud liquid water fraction likely ranges between 0.12 and
239 0.45, which is also higher than the simulated value.

3.2 Cloud phase partition

241   The observed COMBLE MCAOs undergo a distinct cloud phase transition (Fig. 2).
242 In the upstream overcast cloud deck region, satellite lidar-based retrievals identify the
243 cloud top phase as supercooled liquid and the combined lidar-radar retrievals further con-
244 firm the whole cloud layer to be mixed-phase, similar to the findings in the Arctic of a
245 supercooled layer at the top of stratocumulus clouds with continuous ice particles be-
246 low the liquid cloud base (Jackson et al., 2012; Klein et al., 2009; Verlinde et al., 2007).
247 In the downstream cloud streets and cumulus regimes (Fig. 1g,h), both the satellite cloud-
248 top and whole-cloud phase retrievals indicate more dominance of cloud ice (Fig. 2), which
249 is also supported by the ground-based ARM observation (Fig. 1h,i).

250   The SCREAMv0 simulated MCAO clouds reproduce a similar transition from the
251 upstream mixed-phase clouds with a supercooled liquid layer near the cloud top to the
252 downstream ice-dominated cumulus (Fig. 1h,i and Fig. 3a). In terms of IWP and LWP,
253 SCREAMv0 clouds are dominated by ice, particularly for cloud streets and scattered cu-
254 mulus (Fig. 1h,i and Fig. 3a). The modeled cumulus top heights are lower with warmer
255 cloud-top temperatures than the observed (Fig. 1g and Fig. 5g). Even so, the SCREAMv0
256 LWP is much lower, e.g., below the 25th percentile of ARM LWPs(Fig. 1i). This leads
257 to cloud liquid water fraction lower than the $25th$ percentile of ARM data (Fig. 1 h).
258 To further assess the SCREAMv0 cloud phase partition and its relationship to dynam-
259 ics and temperature, we focus on two relationships between: 1) model-resolved updraft
260 and cloud IWP and LWP respectively, 2) cloud liquid water faction and cloud-top tem-
261 perature. As aforementioned, these analyses adopt 3-hourly instantaneous model out-
262 puts of SCREAMv0 Day 33 and 34, and observations of five selected days for statisti-
263 cal robustness.

264   On the dynamic impact, Fig. 4 presents the joint probability distribution function
265 (PDF) between the peak model-resolved vertical velocity below cloud tops and IWP and
266 LWP respectively for BL clouds. The peak model-resolved vertical velocity represents
267 the maximum absolute vertical velocity value beneath the cloud top, specifically at the
268 highest level where $q_i + q_c \geq 1e^{-4} g/kg$. This peak model-resolved vertical velocity cor-

responds to in-cloud updrafts and downdrafts(Fig. 3e,f) associated with the secondary flow of roll and cell convection (Brümmer, 1999; Yang & Geerts, 2006). The cloud streets with high IWP and LWP values (e.g., top 10% and 1% percentile) were found to be mainly collocated with updrafts (Fig. 4e,f). Although grid-boxes with high cloud liquid water fraction mainly locate around cloud edges in cloud streets and cumulus regimes (Fig. 3a), a very small portion ($\leq$ 0.01 Joint-PDF value) of high IWPs ($\geq 200g/m^2$) in the cumulus cloud regime is found in downdrafts (Fig. 4g), likely around the edges of deeper cumulus clouds (Fig. 3a,b,e). Previous observational studies using ground-based data found strong correlations between vertical velocity and both IWP and LWP in Arctic mixed-phase stratiform clouds (Shupe et al., 2008) and between the cloud liquid water and updrafts in COMBLE MCAO cumulus clouds (Mages et al., 2023). Air-borne flight data indicate no evidence of cloud ice collocating with strong updrafts in the Southern Ocean cumulus clouds (Hu, Geerts, et al., 2023). Therefore, further process-oriented modeling studies and more observational evidence are needed to fully understand the strong correlations between updrafts and IWP/LWP found in SCREAMv0.

On the temperature impact, Fig. 5 presents the joint-PDFs between cloud liquid water fraction and cloud-top temperature in the three cloud regimes shown in Fig. 4a,b. To compare model and observation, we further assume correspondences between the phase identification and the value of cloud liquid water fraction: ice for less than 0.1, liquid for greater than 0.9, and mixed-phase for between 0.1 and 0.9. Compared with observations, the SCREAMv0 PDFs show less frequent liquid-phase clouds across all regimes, especially those with cloud-top temperature $\leq -15^oC$. In cloud streets and scattered cumulus regimes with cloud-top temperature $\leq -25^oC$, there are a notable portion of mixed-phase clouds in both satellite and ARM observations (Fig. 5 c and g). However, SCREAMv0 indicates shows all ice-phase clouds (Fig. 5 f), despite the limited presence of SCREAM-modeled clouds with cloud-top temperatures of $\leq -25^oC$, primarily due to insufficient cloud depth. The cloud-top phase partitioning from satellite retrievals and the model estimates (Fig. S6) also suggests that cloud-top supercooled water is underestimated in SCREAMv0 for cloud-top temperature $\leq -15^oC$. Since the ice initiation and production processes are primarily temperature dependent in model microphysics schemes (e.g., Field et al., 2014; Morrison & Milbrandt, 2015; Hu, Geerts, et al., 2023), more in-depth sensitivity tests are needed to understand such discrepancies.

It is worth noting that the assumed SCREAM cloud phase partitioning mentioned above is considered rudimentary and arbitrary. Consequently, it may not effectively capture the subtle sensitivity of various satellite cloud phase retrieval algorithms to cloud microphysics (D. Zhang et al., 2010). Ideally, more realistic satellite simulators should be employed (e.g., Y. Zhang et al., 2019), but they are not available in this SCREAMv0 simulation.

4 Summary

This study evaluates the performance of a global storm resolving model, SCREAMv0, in representing the transition of cloud morphology, and cloud phase partitioning during MCAO events against both satellite and ground-based observations collected in the North Atlantic during the ARM COMBLE field campaign.

On MCAO cloud morphology, SCREAMv0 captures the cloud mesoscale variability: solid stratiform clouds off sea-ice edge, cloud streets over open oceans and scattered cumulus clouds near the Norwegian coast. Accompanying the cloud transition, SCREAMv0 captures the deepening of PBL and intensification of circulations that support cloud streets. However, when compared to observations, SCREAMv0 falls short in reproducing roll cloud structures near the sea-ice edge, and it exhibits much larger horizontal spacing between cloud streets $\sim 500km$ downstream. This discrepancy is partly due to SCREAMv0's effective resolution and should improve with higher model resolution.

Using samples from multiple observed and modeled MCAO days, we found that SCREAMv0 underestimates the cloud liquid water fraction in regimes of cloud streets and scattered cumulus, even with much warmer cloud-top temperatures than the observed. In addition, the high values of cloud IWP and LWP positively correlate with the resolved-scale updrafts in SCREAMv0, indicating that cloud ice and liquid condensates are mainly generated in the mesoscale updrafts for the cloud streets and scatter cumulus regimes. Based on joint PDFs between cloud liquid water fraction and cloud-top temperature, SCREAMv0 underestimates the occurrence of supercooled clouds for cloud-top temperatures ranging from $-15\ to\ -30^oC$ when compared with both satellite and ARM data. Such temperature range is much higher than the typical temperature needed for homogeneous freezing ($\leq -38^oC$). One possibility is that the SCREAMv0 treatment of the Wegener–Bergeron–Findeisen (WBF) process in mixed-phase clouds might be too efficient, e.g., the assumed maximum vertical overlap between liquid and ice for WBF might unrealistically enhance the liquid-to-ice transition (Caldwell et al., 2021). Another possibility is that the prescribed aerosols in SCREAMv0 might provide overabundant Ice Nuclei (IN) without sufficient depletion processes. As a result, when air masses are carried by model-resolved updrafts to height levels close to condensation, there are sufficient IN and water for cloud ice to grow and induce other processes for further ice-phase growth within and below the cloud layer (Hu, Geerts, et al., 2023; Shupe et al., 2008). Testing these hypothesis is a target for future work.

Due to the limited 40-day SCREAMv0 global run, our analysis is based on two days of a simulated MCAO event and five observed MCAO days with similar large-scale conditions. Meanwhile, satellite cloud phase retrievals and the ARM ground-based cloud ice retrieval are challenging for heterogeneous mixed-phase clouds, with considerable uncertainties to be better quantified (Marchant et al., 2020; Ahn et al., 2018; Hu, Geerts, et al., 2023; Deng et al., 2022). A future comprehensive analysis using more MCAO cases, improved retrievals and model satellite simulators could help reduce sampling biases. In addition, we will investigate the impacts of prescribed aerosols and simplified mixed-phase cloud microphysics in SCREAMv0 using the Doubly Periodic configuration of SCREAM (DP-SCREAM) (P. A. Bogenschutz et al., 2023) and Regionally Refined Model configuration of SCREAM (RRM-SCREAM) that simulates a portion of the globe at the kilometer-resolution and leaves the remaining area at coarse-resolution for computational efficiency. Hopefully such process-level sensitivity study against high quality observations will help improve SCREAM in detailed representations of the MCAO mixed-phased cloud transition.

Open Research

The SCREAMv0 output used in this study is publicly available as part of the DYA-MOND2 intercom- parison as described at `https://www.esiwace.eu/services/dyamond`. The code base for this global SCREAMv0 simulation is available at `https://github.com/E3SM-Project/scream/releases/tag/SCREAMv0`.

All the ARM and satellite data downloaded for this study are archived and available online through the NERSC Science Gateways `https://portal.nersc.gov/project/mp193/xzheng/COMBLE/`. For the original data source, all ARM observational data sets used in this study are publicly available from the ARM data archive site (`https://adc.arm.gov/discovery/#/results/iopShortName::amf2019comble/datastream::anxarmbeatmM1.c1/datastream::anxarmbecldradM1.c1/datastream::anxarsclkazr1kolliasM1.c0`). MODIS MOD06_L2 cloud product are publicly available from (`https://ladsweb.modaps.eosdis.nasa.gov/missions-and-measurements/products/MOD06_L2`, DOI:10.5067/MODIS/MOD06_L2.061). CloudSat products can be ordered from the CloudSat Data Processing center (`https://www.cloudsat.cira.colostate.edu/order/`). To download CloudSat data, a new user must first create an account by filling out the signup form (`https://www.cloudsat.cira.colostate.edu/accounts/signup/`).

ERA5 hourly data on single levels and pressure levels are downloaded from Copernicus Climate Change Service (C3S) Climate Data Store (CDS). (Hersbach, Bell, Berrisford, Biavati, et al., 2023; Hersbach, Bell, Berrisford, P., et al., 2023).
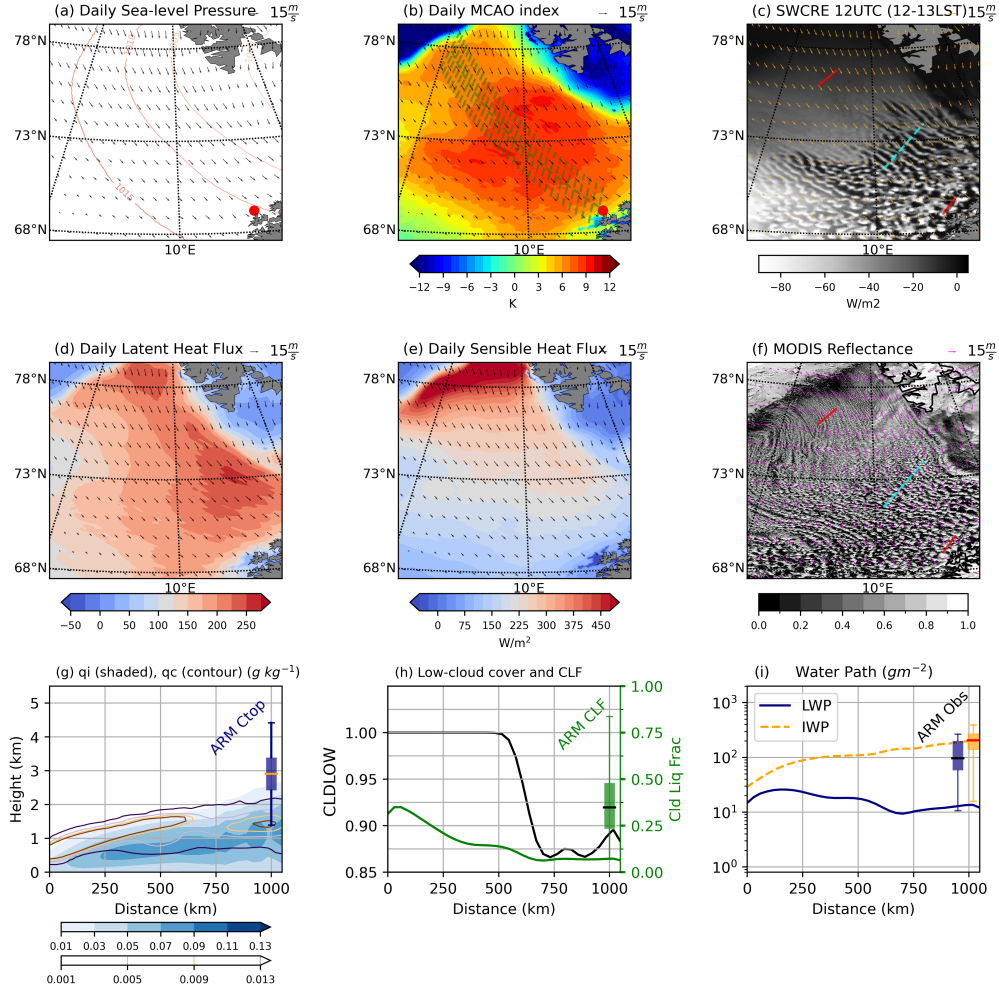
Figure 1. SCREAMv0 MCAO event on Day 34: daily-mean map of (a) sea level pressure (hPa) and (b) MCAO index (K); (c) snapshot of shortwave cloud radiative effect (Wm^{-2}) with near surface wind at 1200UTC (12-13LST); daily-mean map of surface (d) latent heat flux (Wm^{-2}), and (e) sensible heat flux (Wm^{-2}) with near surface wind field over the COMBLE region. (f) MODIS reflectance with ERA5 near surface wind (vectors, ms^{-1}) on 28 March 2020 around 1100UTC. On (c) and (f), the red lines are 100-km reference lines and the cyan dashed line is a 300-km reference line. The location of the ARM AMF1 site is marked as a red dot on (a) and (b). The vertical cross section of daily-mean (g) cloud ice condensate (shaded, gkg^{-1}), cloud liquid condensate (contours,gkg^{-1}) within the band of green dashed lines on (b), and plotted as a function of fetch from the Arctic ice edge. The variability range of the ARM observed hourly cloud top height on 28 March 2020 is shown as navy box-whiskers. (h) Daily-mean low-level cloud cover and cloud liquid water fraction (CLF), along with the variability range of the ARM hourly cloud liquid water fraction (green box-whiskers). (i) Daily-mean IWP (orange dashed) and LWP (navy) (gm^{-2}) within the green dashed band in (b), along with the variability range of the ARM observed hourly IWP (orange box-whisker) and LWP (blue box-whisker). Box and whiskers show $25th$, median, $75th$, $5th$, and $95th$ percentile of the hourly observational data.
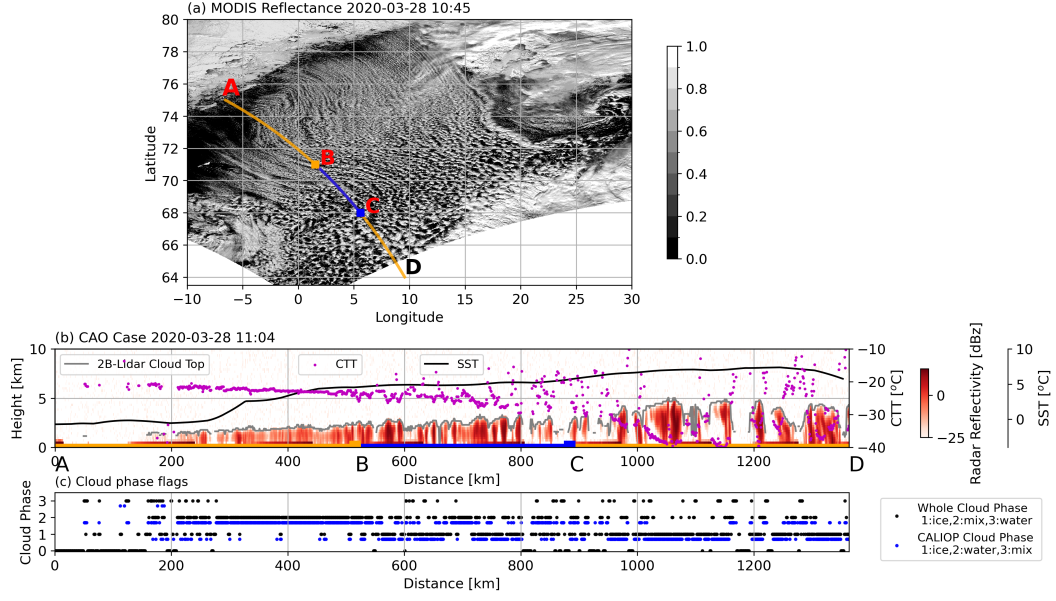
Figure 2. (a) MODIS reflectance during the MCAO event on March 28, 2020. The orange-blue-orange line from Greenland to Norway indicates the path of CALIOP and CloudSat measurements shown in (b) and (c). (b) Vertical cloud structure across the cloud field during the MCAO event sampled by CALIOP and CloudSat, including CloudSat radar reflectivity (shaded), CALIOP lidar cloud top height (gray solid line), sea surface temperature (ECMWF-AUX, black), and CALIOP cloud top temperature retrieval (magenta dots). The orange-blue-orange line, along with corresponding letters, represents the path and locations in (a). (c) CALIOP cloud top phase retrieval (blue dots) and satellite lidar-radar combined whole cloud phase retrieval (black dots). Note that CALIOP cloud top phase retrievals are shifted by -0.3 km for clarity.
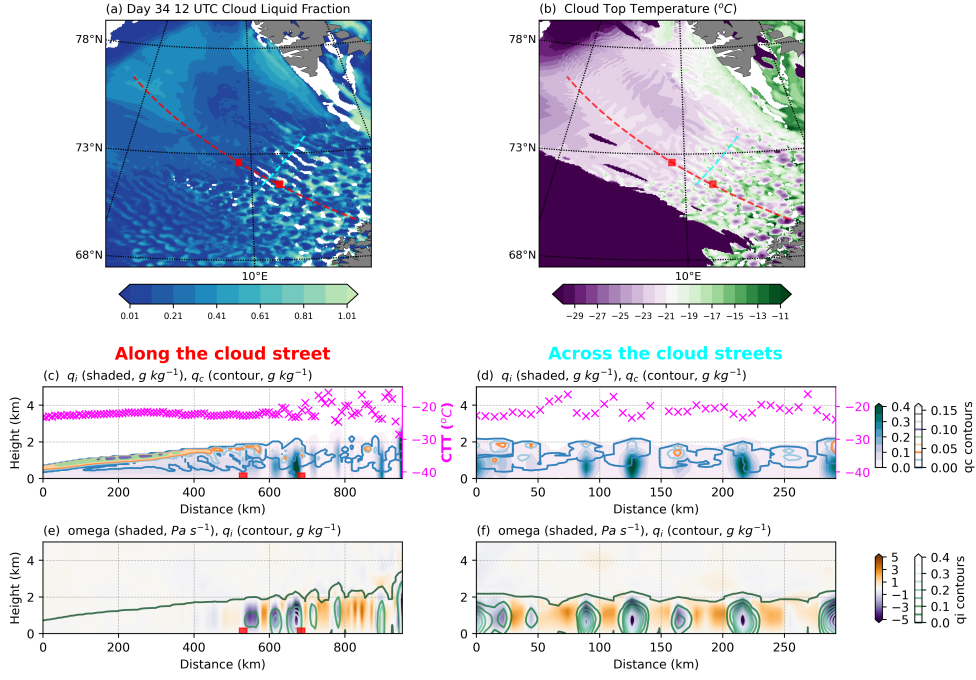
Figure 3. Snapshot of the SCREAMv0 simulated (a) cloud liquid water fraction and (b) cloud top temperature over the COMBLE region on Day 34 at 1200UTC (12-13LST). The vertical cross section of (c) cloud ice condensate (shaded), cloud liquid condensate (contours), and cloud top temperature (magenta symbols) and (e) resolved omega vertical velocity (shaded) and cloud ice condensate (contours) along the cloud street marked as the red dash line in (a-b). (d) and (f) represent the same as (c) and (e) but across the cloud stress (cyan dashed line in a-b and Fig. 1c,f). The start and end of the cloud street, determined by the shortwave cloud radiative effect, are marked by red squares on (c) and (e). The y-axis in (c-f) is the geopotential height estimated from surface pressure, temperature and humidity.
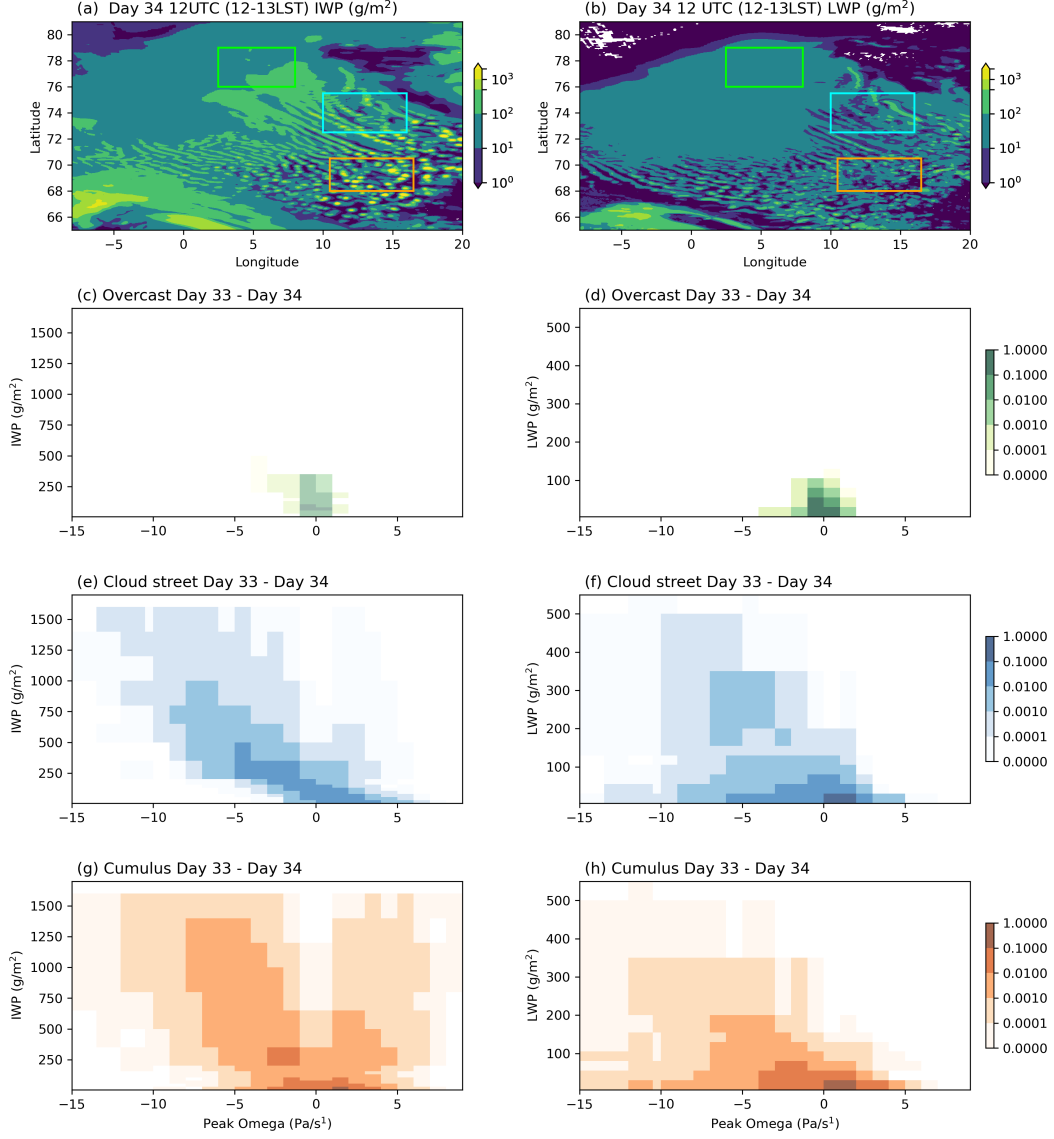
Figure 4. Snapshot of SCREAMv0 (a) IWP and (b) LWP on Day 34 at 1200UTC. Joint-PDF of the 3-hourly instantaneous model-resolved updraft and (left) IWP and (right) LWP during Day 33 and Day 34 over three areas as shown in (a-b). (c-d) Joint PDF for the overcast BL clouds within the green box in (a-b). (e-f) Joint PDF for the cloud streets within the blue box in (a-b). (g-h) Joint PDF for the scattered cumulus clouds within the orange box in (a-b).
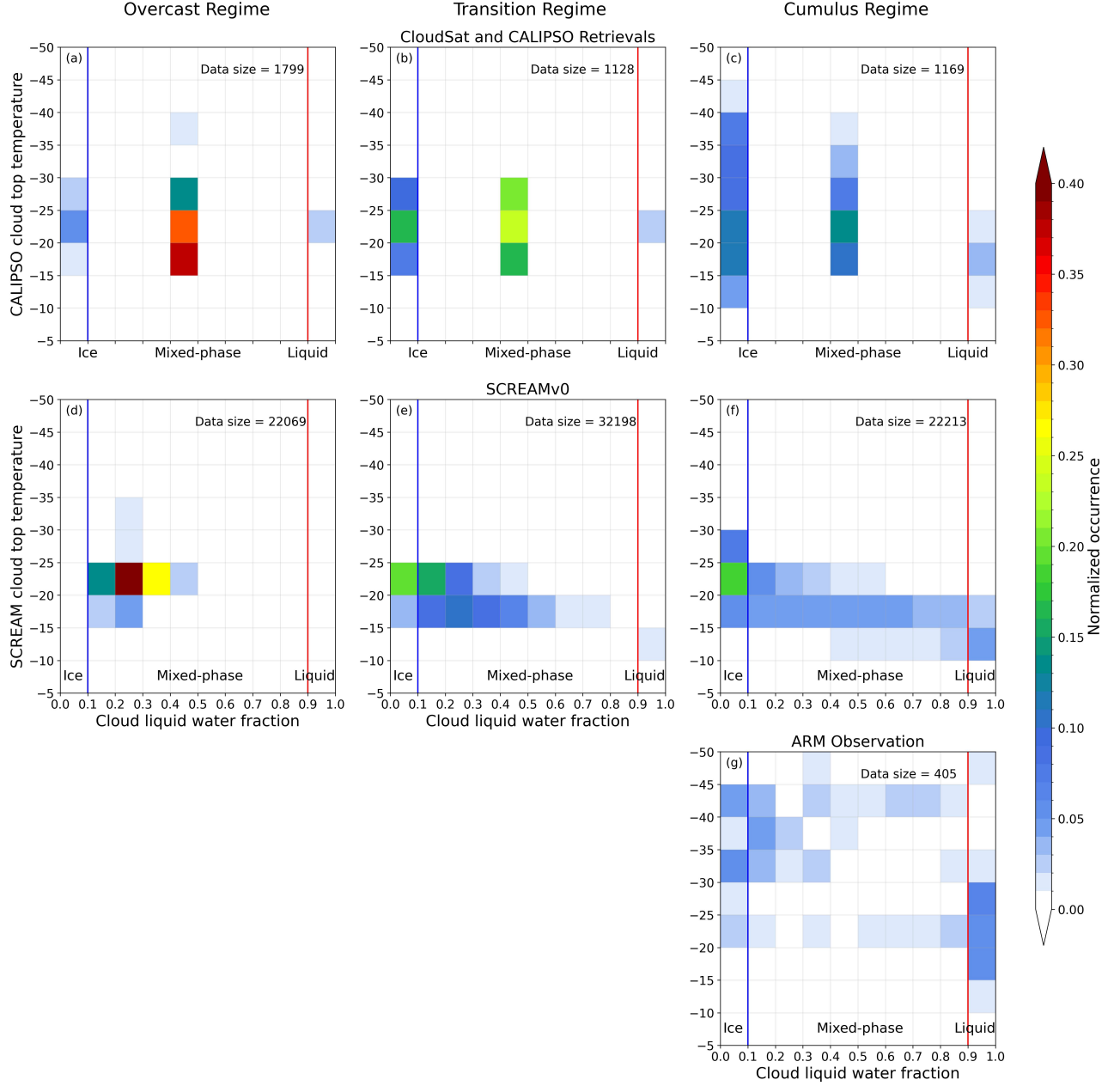
Figure 5. Joint-PDFs of the satellite lidar-radar combined cloud phase retrievals vs. cloud top temperature from 19, 20, 27, 28, 29 March 2020 for (a) overcast cloud regime, (b) transition regime corresponding to the modeled cloud street region, and (c) scattered cumulus cloud regime as shown in Fig. 2 and Fig. S5. Joint-PDFs of the SCREAMv0 cloud liquid water fraction vs. cloud top temperature on Day 33-34 at 0900UC and 1200UTC for the (d) overcast region, (e) cloud street region, and (f) scattered cumuli region as shown in Fig. 4(a). (g) Joint-PDF of observed cloud liquid water fraction vs. cloud top temperature at the ARM AMF1 site on 19, 20, 27, 28, 29 March 2020.

References

Ahn, E., Huang, Y., Siems, S. T., & Manton, M. J. (2018). A comparison of cloud microphysical properties derived from modis and calipso with in situ measurements over the wintertime southern ocean. *Journal of Geophysical Research: Atmospheres*, *123*(19), 11,120-11,140. Retrieved from `https://agupubs.onlinelibrary.wiley.com/doi/abs/10.1029/2018JD028535` doi: https://doi.org/10.1029/2018JD028535

Bogenschutz, P., & Krueger, S. K. (2013). A simplified PDF parameterization of subgrid-scale clouds and turbulence for cloud-resolving models. *Journal of Advances in Modeling Earth Systems*, *5*(2), 195-211. doi: https://doi.org/10.1002/jame.20018

Bogenschutz, P. A., Eldred, C., & Caldwell, P. M. (2023). Horizontal resolution sensitivity of the simple convection-permitting e3sm atmosphere model in a doubly-periodic configuration. *Journal of Advances in Modeling Earth Systems*, *15*(7), e2022MS003466. Retrieved from `https://agupubs.onlinelibrary.wiley.com/doi/abs/10.1029/2022MS003466` (e2022MS003466 2022MS003466) doi: https://doi.org/10.1029/2022MS003466

Brümmer, B. (1999). Roll and cell convection in wintertime arctic cold-air outbreaks. *Journal of the Atmospheric Sciences*, *56*(15), 2613 - 2636. Retrieved from `https://journals.ametsoc.org/view/journals/atsc/56/15/1520-0469_1999_056_2613_racciw_2.0.co_2.xml` doi: https://doi.org/10.117/1520-0469(1999)056⟨2613:RACCIW⟩2.0.CO;2

Cadeddu, M. P., Liljegren, J. C., & Turner, D. D. (2013). The atmospheric radiation measurement (arm) program network of microwave radiometers: instrumentation, data, and retrievals. *Atmospheric Measurement Techniques*, *6*(9), 2359–2372. Retrieved from `https://amt.copernicus.org/articles/6/2359/2013/` doi: 10.5194/amt-6-2359-2013

Caldwell, P. M., Terai, C. R., Hillman, B., Keen, N. D., Bogenschutz, P., Lin, W., ... Zender, C. S. (2021). Convection-permitting simulations with the e3sm global atmosphere model. *Journal of Advances in Modeling Earth Systems*, *13*(11), e2021MS002544. Retrieved from `https://agupubs.onlinelibrary.wiley.com/doi/abs/10.1029/2021MS002544` (e2021MS002544 2021MS002544) doi: https://doi.org/10.1029/2021MS002544

Deng, M., French, J., Geerts, B., Haimov, S., Oolman, L., Plummer, D., & Wang, Z. (2022). Retrieval and evaluation of ice water content from the airborne wyoming cloud radar in orographic wintertime clouds during snowie. *Journal of Atmospheric and Oceanic Technology*, *39*(2), 207 - 221. Retrieved from `https://journals.ametsoc.org/view/journals/atot/39/2/JTECH-D-21-0085.1.xml` doi: https://doi.org/10.1175/JTECH-D-21-0085.1

Field, P. R., Brozkova, R., Chen, M., Dudhia, J., Lac, C., Hara, T., ... McTaggart-Cowan, R. (2017). Exploring the convective grey zone with regional simulations of a cold air outbreak. *Quarterly Journal of the Royal Meteorological Society*, *143*(707), 2537-2555. Retrieved from `https://rmets.onlinelibrary.wiley.com/doi/abs/10.1002/qj.3105` doi: https://doi.org/10.1002/qj.3105

Field, P. R., Cotton, R. J., McBeath, K., Lock, A. P., Webster, S., & Allan, R. P. (2014). Improving a convection-permitting model simulation of a cold air outbreak. *Quarterly Journal of the Royal Meteorological Society*, *140*(678), 124-138. Retrieved from `https://rmets.onlinelibrary.wiley.com/doi/abs/10.1002/qj.2116` doi: https://doi.org/10.1002/qj.2116

Fletcher, J. K., Mason, S., & Jakob, C. (2016). The climatology, meteorology, and boundary layer structure of marine cold air outbreaks in both hemispheres. *Journal of Climate*, *29*(6), 1999 - 2014. Retrieved from `https://journals.ametsoc.org/view/journals/clim/29/6/jcli-d-15-0268.1.xml`

doi: 10.1175/JCLI-D-15-0268.1

Forbes, R. M., & Ahlgrimm, M. (2014). On the representation of high-latitude boundary layer mixed-phase cloud in the ecmwf global model. *Monthly Weather Review*, *142*(9), 3425 - 3445. Retrieved from `https://journals.ametsoc.org/view/journals/mwre/142/9/mwr-d-13-00325.1.xml` doi: https://doi.org/10.1175/MWR-D-13-00325.1

Geerts, B., Giangrande, S. E., McFarquhar, G. M., Xue, L., Abel, S. J., Comstock, J. M., . . . Wu, P. (2022). The comble campaign: A study of marine boundary layer clouds in arctic cold-air outbreaks. *Bulletin of the American Meteorological Society*, *103*(5), E1371 - E1389. Retrieved from `https://journals.ametsoc.org/view/journals/bams/103/5/BAMS-D-21-0044.1.xml` doi: 10.1175/BAMS-D-21-0044.1

Gryschka, M., & Raasch, S. (2005). Roll convection during a cold air outbreak: A large eddy simulation with stationary model domain. *Geophysical Research Letters*, *32*(14). Retrieved from `https://agupubs.onlinelibrary.wiley.com/doi/abs/10.1029/2005GL022872` doi: https://doi.org/10.1029/2005GL022872

Hersbach, H., Bell, B., Berrisford, P., Biavati, G., Horányi, A., . . . Thépaut, J.-N. (2023). Era5 hourly data on pressure levels from 1940 to present. *Copernicus Climate Change Service (C3S) Climate Data Store (CDS)*. doi: 10.24381/cds.bd0915c6(Accessedon28-10-2023)

Hersbach, H., Bell, B., Berrisford, P., Biavati, G., Horányi, A., Muñoz Sabater, J., . . . Thépaut, J.-N. (2023). Era5 hourly data on pressure levels from 1940 to present. *Copernicus Climate Change Service (C3S) Climate Data Store (CDS)*. doi: 10.24381/cds.bd0915c6(Accessedon28-10-2023)

Holdridge, D. (2020, 11). Balloon-borne sounding system (sonde) instrument handbook. *US Department of Energy*. Retrieved from `https://www.osti.gov/biblio/1020712` doi: 10.2172/1020712

Hu, Y., Geerts, B., Deng, M., Grasmick, C., Wang, Y., Lackner, C. P., . . . Zhang, D. (2023). Vertical structure and ice production processes of shallow convective postfrontal clouds over the southern ocean in marcus. part i: Observational study. *Journal of the Atmospheric Sciences*, *80*(5), 1285 - 1306. Retrieved from `https://journals.ametsoc.org/view/journals/atsc/80/5/JAS-D-21-0243.1.xml` doi: https://doi.org/10.1175/JAS-D-21-0243.1

Hu, Y., Lebo, Z. J., Geerts, B., Wang, Y., & Hu, Y. (2023). Vertical structure and ice production processes of shallow convective postfrontal clouds over the southern ocean in marcus. part ii: Modeling study. *Journal of the Atmospheric Sciences*, *80*(5), 1307 - 1327. Retrieved from `https://journals.ametsoc.org/view/journals/atsc/80/5/JAS-D-21-0272.1.xml` doi: https://doi.org/10.1175/JAS-D-21-0272.1

Jackson, R. C., McFarquhar, G. M., Korolev, A. V., Earle, M. E., Liu, P. S. K., Lawson, R. P., . . . Freer, M. (2012). The dependence of ice microphysics on aerosol concentration in arctic mixed-phase stratus clouds during isdac and m-pace. *Journal of Geophysical Research: Atmospheres*, *117*(D15). Retrieved from `https://agupubs.onlinelibrary.wiley.com/doi/abs/10.1029/2012JD017668` doi: https://doi.org/10.1029/2012JD017668

Klein, S. A., McCoy, R. B., Morrison, H., Ackerman, A. S., Avramov, A., Boer, G. d., . . . Zhang, G. (2009). Intercomparison of model simulations of mixed-phase clouds observed during the /arm mixed-phase arctic cloud experiment. i: single-layer cloud. *Quarterly Journal of the Royal Meteorological Society*, *135*(641), 979-1002. Retrieved from `https://rmets.onlinelibrary.wiley.com/doi/abs/10.1002/qj.416` doi: https://doi.org/10.1002/qj.416

Kollias, P., Miller, M. A., Luke, E. P., Johnson, K. L., Clothiaux, E. E., Moran, K. P., . . . Albrecht, B. A. (2007). The atmospheric radiation measurement program cloud profiling radars: Second-generation sampling strategies, process-

ing, and cloud data products. *Journal of Atmospheric and Oceanic Technology*, *24*(7), 1199 - 1214. Retrieved from https://journals.ametsoc.org/view/journals/atot/24/7/jtech2033_1.xml doi: https://doi.org/10.1175/JTECH2033.1

Lloyd, G., Choularton, T. W., Bower, K. N., Gallagher, M. W., Crosier, J., O'Shea, S., ... Boutle, I. A. (2018). In situ measurements of cloud microphysical and aerosol properties during the break-up of stratocumulus cloud layers in cold air outbreaks over the north atlantic. *Atmospheric Chemistry and Physics*, *18*(23), 17191–17206. Retrieved from https://acp.copernicus.org/articles/18/17191/2018/ doi: 10.5194/acp-18-17191-2018

Ma, H.-Y., Xie, S., Klein, S. A., Williams, K. D., Boyle, J. S., Bony, S., ... Williamson, D. (2014). On the correspondence between mean forecast errors and climate errors in cmip5 models. *Journal of Climate*, *27*(4), 1781 - 1798. Retrieved from https://journals.ametsoc.org/view/journals/clim/27/4/jcli-d-13-00474.1.xml doi: https://doi.org/10.1175/JCLI-D-13-00474.1

Mages, Z., Kollias, P., Zhu, Z., & Luke, E. P. (2023). Surface-based observations of cold-air outbreak clouds during the comble field campaign. *Atmospheric Chemistry and Physics*, *23*(6), 3561–3574. Retrieved from https://acp.copernicus.org/articles/23/3561/2023/ doi: 10.5194/acp-23-3561-2023

Marchand, R., Mace, G. G., Ackerman, T., & Stephens, G. (2008). Hydrometeor detection using cloudsat—an earth-orbiting 94-ghz cloud radar. *Journal of Atmospheric and Oceanic Technology*, *25*(4), 519 - 533. Retrieved from https://journals.ametsoc.org/view/journals/atot/25/4/2007jtecha1006_1.xml doi: 10.1175/2007JTECHA1006.1

Marchant, B., Platnick, S., Meyer, K., & Wind, G. (2020). Evaluation of the modis collection 6 multilayer cloud detection algorithm through comparisons with cloudsat cloud profiling radar and calipso caliop products. *Atmospheric Measurement Techniques*, *13*(6), 3263–3275. Retrieved from https://amt.copernicus.org/articles/13/3263/2020/ doi: 10.5194/amt-13-3263-2020

McCoy, I. L., Wood, R., & Fletcher, J. K. (2017). Identifying Meteorological Controls on Open and Closed Mesoscale Cellular Convection Associated with Marine Cold Air Outbreaks. *Journal of Geophysical Research: Atmospheres*, *122*, 11,678–11,702. doi: https://doi.org/10.1002/2017JD027031

Morrison, H., & Milbrandt, J. A. (2015). Parameterization of cloud microphysics based on the prediction of the bulk ice particle properties. part i: Scheme description and idealized tests. *J. Atmos. Sci.*, *72*, 287–311.

Naud, C. M., Booth, J. F., Jeyaratnam, J., Donner, L. J., Seman, C. J., Zhao, M., ... Ming, Y. (2019). Extratropical cyclone clouds in the gfdl climate model: Diagnosing biases and the associated causes. *Journal of Climate*, *32*(20), 6685 - 6701. Retrieved from https://journals.ametsoc.org/view/journals/clim/32/20/jcli-d-19-0421.1.xml doi: https://doi.org/10.1175/JCLI-D-19-0421.1

Neumann, P., Düben, P., Adamidis, P., Bauer, P., Brück, M., Kornblueh, L., ... Biercamp, J. (2019). Assessing the scales in numerical weather and climate predictions: will exascale be the rescue? *Philosophical Transactions of the Royal Society A: Mathematical, Physical and Engineering Sciences*, *377*(2142), 20180148. Retrieved from https://royalsocietypublishing.org/doi/abs/10.1098/rsta.2018.0148 doi: 10.1098/rsta.2018.0148

Papritz, L., & Spengler, T. (2017). A lagrangian climatology of wintertime cold air outbreaks in the irminger and nordic seas and their role in shaping air–sea heat fluxes. *Journal of Climate*, *30*(8), 2717 - 2737. Retrieved from https://journals.ametsoc.org/view/journals/clim/30/8/jcli-d-16-0605.1.xml doi: 10.1175/JCLI-D-16-0605.1

Pithan, F., Svensson, G., Caballero, R., Chechin, D., Cronin, T. W., Ekman,

A. M. L., . . . Wendisch, M. (2018). Role of air-mass transformations in exchange between the arctic and mid-latitudes. *Nature Geoscience*, *11*, 805 - 812. Retrieved from https://doi.org/10.1038/s41561-018-0234-1 doi: 10.1038/s41561-018-0234-1

Sassen, K., Wang, Z., & Liu, D. (2008). Global distribution of cirrus clouds from cloudsat/cloud-aerosol lidar and infrared pathfinder satellite observations (calipso) measurements. *Journal of Geophysical Research: Atmospheres*, *113*(D8). Retrieved from https://agupubs.onlinelibrary.wiley.com/doi/abs/10.1029/2008JD009972 doi: https://doi.org/10.1029/2008JD009972

Satoh, M., Stevens, B., Judt, F., Khairoutdinov, M., Lin, S.-J., Putman, W. M., & Duben, P. (2019). Global cloud-resolving models. *Curr Clim Change Rep*, *5*, 172-184. doi: https://doi.org/10.1007/s40641-019-00131-0

Shupe, M. D., Kollias, P., Persson, P. O. G., & McFarquhar, G. M. (2008). Vertical motions in arctic mixed-phase stratiform clouds. *Journal of the Atmospheric Sciences*, *65*(4), 1304 - 1322. Retrieved from https://journals.ametsoc.org/view/journals/atsc/65/4/2007jas2479.1.xml doi: https://doi.org/10.1175/2007JAS2479.1

Stevens, B., Satoh, M., Auger, L., Biercamp, J., Bretherton, C. S., Chen, X., . . . Zhou, L. (2019). DYAMOND: the DYnamics of the Atmospheric general circulation Modeled On Non-hydrostatic Domains. *Progress in Earth and Planetary Science*, *6*(1), 61. doi: 10.1186/s40645-019-0304-z

Tornow, F., Ackerman, A. S., & Fridlind, A. M. (2021). Preconditioning of overcast-to-broken cloud transitions by riming in marine cold air outbreaks. *Atmospheric Chemistry and Physics*, *21*(15), 12049–12067. Retrieved from https://acp.copernicus.org/articles/21/12049/2021/ doi: 10.5194/acp-21-12049-2021

Verlinde, J., Harrington, J. Y., McFarquhar, G. M., Yannuzzi, V. T., Avramov, A., Greenberg, S., . . . Schofield, R. (2007). The mixed-phase arctic cloud experiment. *Bulletin of the American Meteorological Society*, *88*(2), 205 - 222. Retrieved from https://journals.ametsoc.org/view/journals/bams/88/2/bams-88-2-205.xml doi: 10.1175/BAMS-88-2-205

Wu, P., & Ovchinnikov, M. (2022). Cloud morphology evolution in arctic cold-air outbreak: Two cases during comble period. *Journal of Geophysical Research: Atmospheres*, *127*(10), e2021JD035966. Retrieved from https://agupubs.onlinelibrary.wiley.com/doi/abs/10.1029/2021JD035966 (e2021JD035966 2021JD035966) doi: https://doi.org/10.1029/2021JD035966

Xie, S., McCoy, R. B., Klein, S. A., Cederwall, R. T., Wiscombe, W. J., Jensen, M. P., . . . Turner, D. D. (2010). Clouds and more: Arm climate modeling best estimate data: A new data product for climate studies. *Bulletin of the American Meteorological Society*, *91*(1), 13 - 20. Retrieved from https://journals.ametsoc.org/view/journals/bams/91/1/2009bams2891_1.xml doi: 10.1175/2009BAMS2891.1

Yang, Q., & Geerts, B. (2006). Horizontal convective rolls in cold air over water: Buoyancy characteristics of coherent plumes detected by an airborne radar. *Monthly Weather Review*, *134*(9), 2373 - 2396. Retrieved from https://journals.ametsoc.org/view/journals/mwre/134/9/mwr3203.1.xml doi: https://doi.org/10.1175/MWR3203.1

Zhang, D., Wang, Z., & Liu, D. (2010). A global view of midlevel liquid-layer topped stratiform cloud distribution and phase partition from calipso and cloudsat measurements. *Journal of Geophysical Research: Atmospheres*, *115*(D4). Retrieved from https://agupubs.onlinelibrary.wiley.com/doi/abs/10.1029/2009JD012143 doi: https://doi.org/10.1029/2009JD012143

Zhang, Y., Xie, S., Lin, W., Klein, S. A., Zelinka, M., Ma, P.-L., . . . Ma, H.-Y. (2019). Evaluation of clouds in version 1 of the e3sm atmosphere model with satellite simulators. *Journal of Advances in Modeling Earth Systems*,

617   *11*(5), 1253-1268.   Retrieved from `https://agupubs.onlinelibrary.wiley`
618   `.com/doi/abs/10.1029/2018MS001562`   doi: https://doi.org/10.1029/
619   2018MS001562